Multi-Spectral Solar Telescope Array V: temperature diagnostic response to the optically thin solar plasma

Craig E. DeForest
Charles C. Kankelborg
Max J. Allen
Elizabeth S. Paris
Tom D. Willis
Joakim F. Lindblom, MEMBER SPIE
Ray H. O'Neal
Arthur B. C. Walker, Jr., MEMBER SPIE
Stanford University
Center for Space Science and Astrophysics
Stanford, California 94305

Troy W. Barbee, Jr., MEMBER SPIE
Lawrence Livermore National Laboratory
Livermore, California 94550

Richard B. Hoover, MEMBER SPIE
NASA Marshall Space Flight Center
Space Science Laboratory
Huntsville, Alabama 35812

Troy W. Barbee III
University of California/Berkeley
Berkeley, California 94720

Abstract. We have developed compact soft x-ray, extreme ultraviolet (EUV), and far-ultraviolet (FUV) multilayer coated telescopes for the study of the solar chromosphere, corona, and corona/solar wind interface. Because these systems operate at short wavelengths (~ 40 Å $< \lambda <$ 1550 Å), the modest apertures of 40 to 127 mm allow observations at very high angular resolution (0.1 to 0.7 arcsec). In addition to permitting traditional normal incidence optical configurations (such as Cassegrain, Ritchey-Chrétien, and Herschelian configurations) to be used at soft x-ray/EUV wavelengths, multilayer coatings also allow a narrow wavelength band ($\lambda/\Delta\lambda \sim 15 - 100$) to be selected for imaging. The resulting telescopes provide a very powerful and flexible diagnostic instrument for the study of both the fine-scale structure of the chromosphere/corona interface and the large-scale structure of the corona and corona/solar wind interface. In previous papers, we have described a new solar rocket payload, the Multi-Spectral Solar Telescope Array (MSSTA), which is composed of 17 of these compact telescopes. In the present paper, we report on the ability of the MSSTA payload to obtain temperature diagnostic information about the optically thin solar plasma. We also discuss applications of this information to studies of coronal structure.

Subject terms: x-ray/EUV optics; multilayer optics; solar corona; solar plasma diagnostics.

Optical Engineering 30(8), 1125-1133 (August 1991).

CONTENTS

1. INTRODUCTION

The Multi-Spectral Solar Telescope Array (MSSTA) is a comprehensive rocket-borne solar observatory that is capable of obtaining narrow band images of chromospheric and coronal structures in the soft x-ray, extreme ultraviolet (EUV), and far-ultraviolet (FUV), with very high (0.1 to 0.7 arcsec) angular resolution.[1] Spectral resolution is achieved by the use of an array of compact multilayer coated normal incidence telescopes that are able to achieve a resolving power of $\lambda/\Delta\lambda \sim 15 - 100$. The MSSTA payload includes two Cassegrain, seven Ritchey-Chrétien, and eight Herschelian telescopes, which form images in narrow wavelength bands in the soft x ray, EUV, and FUV. We have previously described the optical design of the Ritchey-Chrétien,[2] Cassegrain,[3] and Herschelian[1] telescopes, as well as the arrangement of the MSSTA telescopes[1] within the 22-in. (56-cm)-diam rocket shroud. In the present paper, we discuss the effectiveness of the MSSTA instrument as a temperature-sensitive diagnostic of the solar coronal plasma.

Invited paper XR-105 received Jan. 10, 1991; revised manuscript received March 15, 1991; accepted for publication March 16, 1991.

2. SOLAR EMISSION

The solar soft x-ray (5 to 100 Å) and EUV (100 to 1000 Å) spectrum arises largely from the upper chromosphere and lower corona, where the scale (typically 70 to 7000 km, or ~0.1 to 10 arcsec as viewed from Earth) and density ($\sim 10^6$ to 10^{10} cm^{-3}) of the structures (coronal loops, spicules, polar plumes, streamers) that dominate the atmosphere are such that they are transparent to most of their own emissions (i.e., optically thin). FUV (1000 to 2000 Å) lines, such as the Lyman α line of H I at 1216 Å, and a few EUV lines, such as He I at 504 Å and He II at 304 Å, can have large optical depths in the chromosphere.[4]

Because each of these lines is emitted by a single species of ion, and different ionization states dominate the plasma at different temperatures, each line is excited in a distinct temperature range. The optics of each MSSTA telescope are designed to be sensitive to a small number of lines that are excited at nearly the same temperature, enabling each telescope to selectively detect plasma in a particular temperature range. Table 1 shows the major emission lines in each of the MSSTA telescope bandpasses, with the temperature of peak emission for each line.

Let $I(\lambda,T(x,y,z),n(x,y,z))dV$ be the power per unit wavelength radiated from the volume element dV at the location x,y,z

TABLE 1. Characteristics of the MSSTA optical systems.

Telescope	Wavelength (Å)	Ion	Mirror Coating	Filter (+) (Thickness in μm)	Bandpass (*) (Å)	Solar Temperature (K)	Focal Length (mm)	Aperture (mm)	Plate Scale (μm/")	f ratio	Solar Image (mm)	Resolution (£)
Ritchey Chrétien XII-A	1216	H I	Al/MgF_2/Os	MgF_2/Al	65	20,000	3500	127	17.0	27.6	32.6	0.24"
Ritchey Chrétien XII-B	1548	C IV	Al/MgF_2/Os	MgF_2/Al	100	100,000	3500	127	17.0	27.6	32.6	0.33"
Ritchey Chrétien XII-C	304	He II	Mo/Mg_2Si	Al (.28)/C(.0125)	18	80,000	3500	127	17.0	27.6	32.6	0.10"
Ritchey Chrétien XII-D	150	O VI	Mo/S	Be(.60)	8	300,000	3500	127	17.0	27.6	32.6	0.33"
Ritchey Chrétien XII-E	173	Fe IX/X	Mo/S	Al (.28)/C(.04)	6	900,000	3500	127	17.0	27.6	32.6	0.33"
Ritchey Chrétien XII-F	193	Fe XII Fe XXIV(§)	Mo/S	Al (.28)/KBr(.16)/Water(.01)	15	1,500,000 20,000,000	3500	127	17.0	27.6	32.6	0.33"
Ritchey Chrétien XII-G	335	Fe XVI	Mo/Mg_2Si	Al (.18)/C(.008)/Te(.14)	23	4,000,000	3500	127	17.0	27.6	32.6	0.33"
Cassegrain VI-a	173	Fe IX/X	Mo/S	Al (.28)/C(.04)	6	1,000,000	2000	60.3	9.7	33.2	18.6	0.50"
Cassegrain VI-b	211	Fe XIV	Mo/S	Al (.28)/KBr(.16)/Water(.01)	14	2,500,000	2000	60.3	9.7	33.2	18.6	0.50"
Herschelian IV-a	143.3	Ne V	Mo/S	Be(.3)/Mo(.28)	7	400,000	1400	40	6.8	35.0	13.0	0.75"
Herschelian IV-b	88.1	Ne VIII	Rh/B_4C	Rh(.08)/C(.0275)/Phth(.0384)/Mo(.28)	4	650,000	1400	40	6.8	35.0	13.0	0.75"
Herschelian IV-c	69.7	Si VIII	Rh/B_4C	Rh(.16)/C(.3638)/Pht(.2358)	2.5	800,000	1400	40	6.8	35.0	13.0	0.75"
Herschelian IV-d	57.9	Mg X	Rh/C	Rh(.16)/C(.3638)/Pht(.2358)	1.4	1,250,000	1400	40	6.8	35.0	13.0	0.75"
Herschelian IV-e	44.1	Si XII	Rh/C	Rh(.16)/C(.3638)/Pht(.2358)	0.6	2,000,000	1400	40	6.8	35.0	13.0	0.75"
Herschelian IV-f	54.7	Fe XVI	Rh/C	Rh(.16)/C(.3638)/Pht(.2358)	1.2	4,000,000	1400	40	6.8	35.0	13.0	0.75"
Herschelian IV-g	93.9	Fe XVIII	Rh/B_4C	Rh(.08)/C(.0275)/Phth(.0384)/Mo(.28)	4	6,000,000	1400	40	6.8	35.0	13.0	0.75"
Herschelian IV-h	132.8	Fe XX Fe XXIII(§)	Mo/S	Be(.3)/Mo(.28)	5	8,000,000 16,000,000	1400	40	6.8	35.0	13.0	0.75"

Notes:
(+) Phth is Phthalocyanine (*) Bandpasses for 173 Å include L-edge of aluminum filter. Number in parentheses are for a single mirror
(§) These high temperature lines are only expected to contain appreciable flux during or shortly after flares
(£) The higher fluxes at 1215.6 Å and 304 Å will allow higher resolution (and hence lower sensitivity) film to be used in these systems. The resolution at 1215.6 Å is diffraction limited, while the resolution at 304 Å is limited by the optics figure. A higher resolution film may be used in some of the other Ritchey-Chrétien sytems, allowing a resolution greater than 0.33" to be achieved.

within the optically thin solar plasma. If one assumes that elemental abundances are the same everywhere in the Sun, I is approximately proportional to the square of the electron density. It is therefore convenient to define the quantity

$$I_n[\lambda,T(x,y,z)] = \frac{I[\lambda,T(x,y,z),n(x,y,z)]}{n_e^2} , \quad (1)$$

where n_e is the electron density, and I is the solar emissivity at a given wavelength and location. We shall henceforth refer to I_n as the "emissivity"; it is (approximately) constant across changes in electron density. The intensity at the film plane of a solar telescope, caused by a solar feature at angular location (x,y), is then given by (neglecting the finite resolution of the telescope)

$$\Phi(x',y') = \frac{\pi}{4} f_{tel}^2 \int_{a/2}^{A/2} dr \int_0^{2\pi} r\, d\theta\, V(r,\theta,x,y) \times \int_0^{\infty} d\lambda \int_{-\infty}^{\infty} ds\, \varepsilon_{tel}(\lambda)\, I_n[\lambda, T(x,y,s)]\, n_e^2(x,y,s) , \quad (2)$$

where r and θ are coordinates on the primary mirror of the telescope; a is the diameter of the central obscuration (zero for a Herschelian); A is the diameter of the primary mirror; $V(r,\theta,x,y)$ is the vignetting function of the telescope; x and y are solar coordinates (which are mapped onto the film coordinates x',y'); s is a coordinate along the line of sight; $\mathbf{f}_{tel}$ is the f ratio of the telescope; and ε_{tel} is the total throughput efficiency of the telescope optics at a given wavelength. Note that the electron density is explicitly included in Eq. (2).

With the approximation that all radiated flux is contained in a finite number of spectral lines that are narrow compared to the telescope bandpass, I_n becomes a sum of delta functions in λ. Letting k arbitrarily label all spectral lines of interest, we find that the λ integral reduces to a sum over k:

$$\Phi(x',y') = \frac{\pi}{4} f_{tel}^2\, \mathbf{V}(x,y) \int_{-\infty}^{\infty} ds \left\{ n_e^2(x,y,z) \sum_k I_{nk}[T(x,y,z)]\, \varepsilon_{tel}(\lambda_k) \right\} , \quad (3)$$

where λ_k is the wavelength of the k'th emission line, I_{nk} is the solar emissivity in the k'th emission line, and $\mathbf{V}(x,y)$ is the vignetting function of the telescope. Further, the integral over s can be rewritten in terms of the temperature distribution along the line of sight, as follows:[5]

$$\Phi(x',y') = \frac{\pi}{4} f_{tel}^2\, \mathbf{V}(x,y) \int_{-\infty}^{\infty} dT_e n_e^2(T_e,x,y)\, K(T_e) , \quad (4)$$

where $n_e^2(T_e)$, the emission measure, is characteristic of the solar structure under study. The "kernel" of the integral $K(T_e)$, which is the convolution of the telescope efficiency and the solar emissivity, is given by a λ sum indexed by element (Z), ionization stage (z), and transition from excited state i to lower state j:

$$K(T_e) = \sum_k I_{nk} \varepsilon_{tel}(\lambda_k) = \sum_{Zzij} A_Z a_{Zz}(T_e) \alpha_{Zzij}(T_e) \varepsilon_{tel}(\lambda_{ij}) , \quad (5)$$

where A_Z is the abundance of element Z, a_{Z_z} is the fractional population of ionization stage z, and α_{Zz} is the excitation function for transition $(i \rightarrow j)$ (including all population processes for the upper level i, and branching ratios to the lower level j). These relations only hold for optically thin lines; thus, this derivation is not valid for the 1216-Å telescope, which is sensitive to the optically thick Lyman α line.[4] However, it is approximately valid for the remainder of the telescopes onboard MSSTA.

We have obtained theoretical calculations of the functions $A_Z a_{Zz}(T_e)\alpha_{Zzij}(T_e)$ from Mewe et al.[6] for lines with [1 Å < λ < 300 Å] and from Landini and Fossi[7] for lines with [300 Å < λ < 2000 Å]. If one uses this data, and the throughput information for a MSSTA telescope, it is possible to evaluate the sum in Eq. (5) to find the response (in incident power density at the film plane) of each telescope to a unit mass of solar plasma, as a function of temperature of the plasma. Conversely, it is possible to design the telescope throughput function $\varepsilon_{tel}(\lambda)$ to achieve maximal temperature resolution for the telescope. Ideally, each telescope would respond strongly to solar plasma in a narrow temperature range, and very weakly to plasma outside that range.

3. DESCRIPTION OF MSSTA OPTICAL SYSTEMS

The telescope throughput $\varepsilon_{tel}(\lambda)$ provides a means of discriminating between different spectral lines, and, thus, between structures at different temperatures in the solar atmosphere. If the throughput of a telescope includes only a small number of lines, temperature selectivity of that telescope will be high; if many lines are admitted, temperature selectivity will be low, and little temperature information will be contained in the image. There are two optical elements in each telescope that provide wavelength selectivity: the multilayer mirrors, which provide a narrow bandpass near the desired wavelength[8] and a thin-film filter, which eliminates offband contamination from specular and high-order reflectivity in the multilayers, and may contribute to the sharpness of the primary bandpass.[9] The overall throughput efficiency of the telescope is the product of the efficiencies of its elements, so that, for a dual-reflection telescope with a filter in place, we can write:

$$\varepsilon_{tel}(\lambda) = \varepsilon_p(\lambda)\varepsilon_s(\lambda)t_f(\lambda) \ , \qquad (6)$$

where ε_p is the reflectivity of the primary mirror, ε_s is the reflectivity of the secondary mirror, and t_f is the transmission of the filter.

The multilayer coatings on the optical surfaces provide sharp bandpass throughput curves near the desired wavelength but admit significant amounts of contaminating radiation at wavelengths far from the primary bandpass. At wavelengths shortward of the primary bandpass, there are second- and higher-order bandpasses at integer harmonics of the desired wavelength, possibly admitting additional multiplets of shorter wavelength lines. At wavelengths much longer than the primary bandpass, specular reflectivity of the coatings dominates the throughput curve; this admits contamination by all sufficiently long-wavelength solar emissions, including visible light (see Fig. 1). In the MSSTA telescopes, thin-film metal filters are used[9] to block out this undesired radiation. The throughput function for each telescope, as defined in Eq. (6), is the product of the reflectivities of all mirrors and filters in the telescope. For the 173-Å telescopes, an additional improvement of spectral selectivity is gained by the use of aluminum in the filter: the aluminum L absorption edge at 171 Å effectively cuts the primary bandpass in half, improving the selectivity of the primary throughput peak.

Another method of improving the spectral selectivity of a multilayer telescope is to use the multilayer in second order. The ideal full-width at half-maximum of the second-order bandpass is half that of the first-order bandpass, because there are twice as many nodes in the standing wave pattern in second order. Thus, a 304-Å multilayer mirror with a $\lambda/\Delta\lambda$ of 20 can be used in second order as a 152-Å element, with a $\lambda/\Delta\lambda$ of roughly 40. There are two main drawbacks to using the second-order peak for the main bandpass: the lower peak reflectivity of the second-order bandpass; and the potential, in double-reflection telescopes, for band mismatch of the two mirrors caused by the narrower bandpass. These problems could be avoided by using a single-reflection (Herschelian) configuration, or by using a hybrid design in which one mirror is operated in second order, while the other is used in first order.

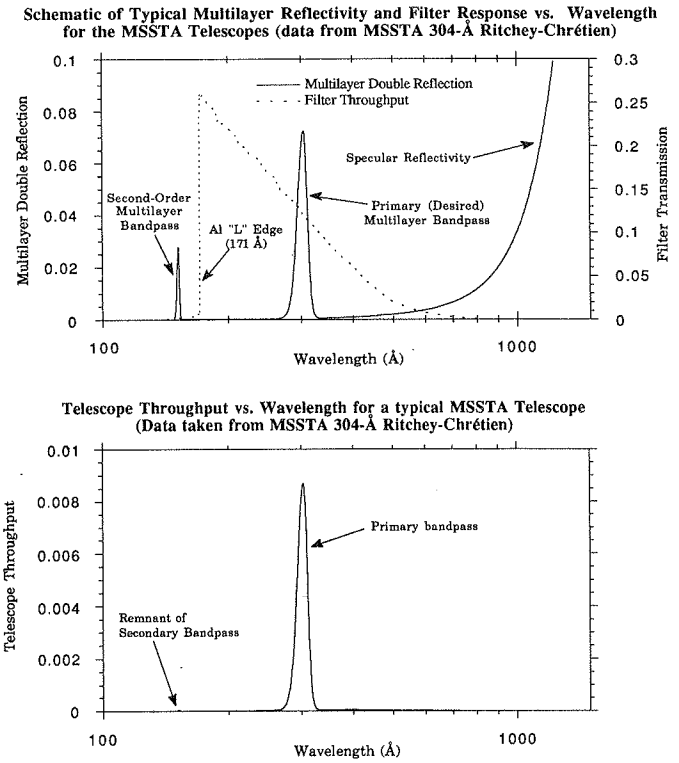

Fig. 1. Schematics of multilayer and filter throughput for a typical MSSTA double-reflection telescope, and of the resulting overall telescope throughput. The total multilayer throughput through both reflections yields a narrow bandpass at the first order peak (304 Å), with a large (undesired) second-order throughput peak at 152 Å and high reflectivity of long wavelengths. The filter makes use of the aluminum "L" absorption edge at 171 Å to cut out the second-order bandpass, resulting in the overall throughput at the bottom.

The bandpasses of the telescopes in the MSSTA were chosen so that the cluster would "see" a variety of spectral lines. Figure 2 shows the predicted reflectivity curves versus wavelength of the MSSTA multilayer telescopes. The curves for the Cassegrain and XUV Ritchey-Chrétien telescopes are based on multilayer reflectivities measured[8] at the Stanford Synchrotron Radiation Laboratory in the spring of 1990, and theoretical filter throughputs.[9] The curves for the Herschelian and FUV Ritchey-Chrétien telescopes are based on theoretical multilayer reflectivities[10] and filter throughput.

4. TEMPERATURE RESPONSE

The utility of an image as a plasma temperature diagnostic is described by the kernel function (Eq. 5). As discussed earlier, we have sufficient information to evaluate the sum in Eq. (5) for each telescope, giving the kernel K from Eq. (4), i.e., the telescope response versus plasma temperature. Figure 3 shows the temperature response kernels for the single- and double-reflection telescopes on the MSSTA.

As can be seen in Fig. 3, many of the actual temperature responses contain significant contributions from other temperatures than the desired one, because of the inclusion of multiple lines. Figure 4 illustrates how multiple lines can affect the response of a telescope: the 93.9-Å Herschelian telescope was designed to respond to the Fe XVIII line at 93.93 Å, which has peak emission at 5×10^6 K. However, two other classes of lines are also included in the bandpass: several Fe lines (primarily an Fe X line at 94.0 Å) which peak at 10^6 K; and some Ne and Mg lines on opposite sides of the bandpass, which contribute to a peak at 5×10^5 K. This results in the trimodal response curve seen at bottom of Fig. 4.

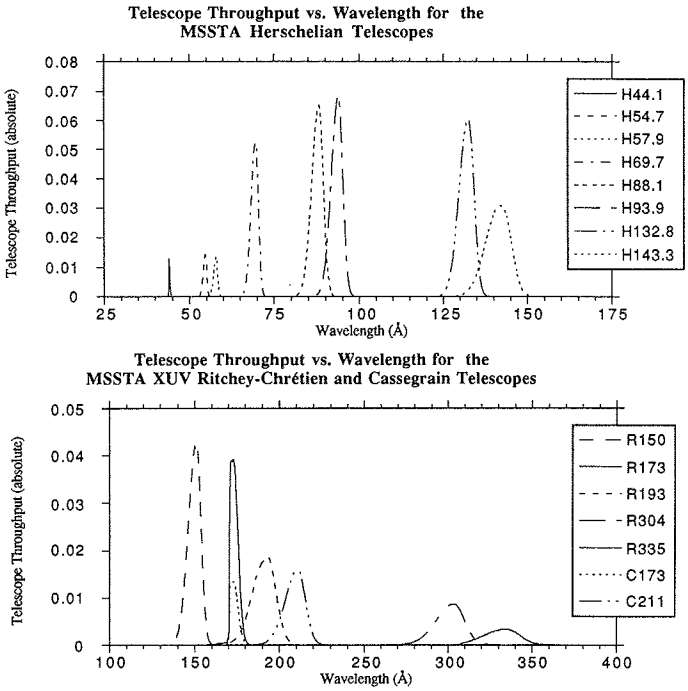

Fig. 2. Bandpass characteristics of the MSSTA multilayer telescopes.

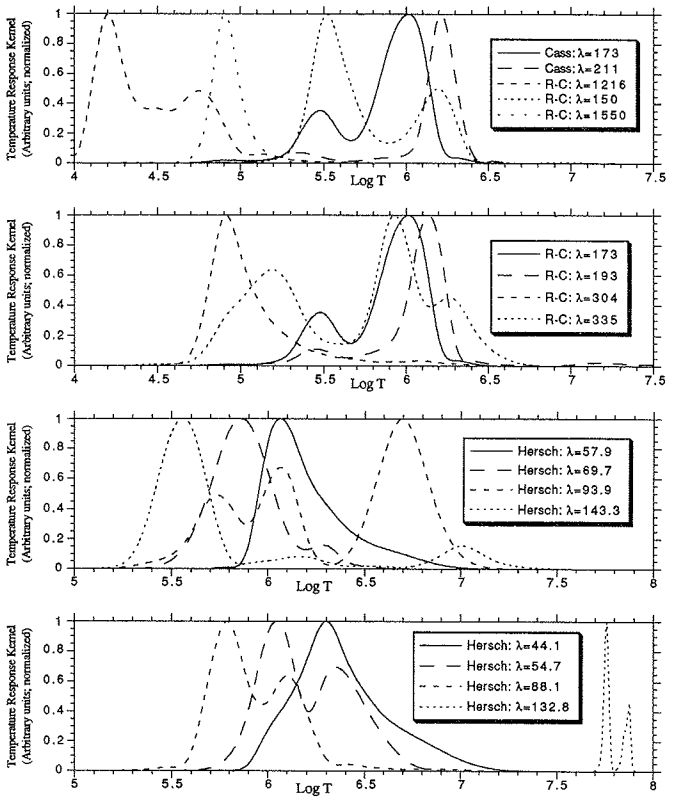

Fig. 3. Temperature response kernels for the MSSTA multilayer telescopes. This data is based on spectral response information calculated by Mewe et al.[6] and Landini and Fossi[7] convolved as in Eq. 5.

The inclusion of many lines in a telescope's bandpass does not necessarily result in poor temperature selectivity for the telescope. For example, consider the MSSTA 193 Å Ritchey-Chrétien telescope, for which the major spectral lines are shown in Fig. 5. There are at least 20 lines that contribute 2% or more of the overall response; however, since most of the lines peak at or near the same temperature, the response curve is still sharp, as seen at bottom of Fig. 5.

Temperature resolution can be considerably improved by reducing contamination during the design phase of a telescope. In general, adjusting the multilayer characteristics of a telescope affects the onband contamination, while modifying the filter characteristics changes the offband characteristics. For example, the 54.7-Å Herschelian telescope, as originally designed, had the temperature response shown in Fig. 6. The chosen line for the telescope was the Fe XVI line at 54.7 Å, which peaks at 3.0×10^6 K. However, there are several other lines in the bandpass, notably an Si IX line at 55.4 Å, which is stronger than the 54.7-Å line, and dominates the temperature response kernel of the telescope. Changing the width of the multilayer bandpass strongly affects the relative strength of the contaminant line in the temperature response kernel. The multilayer reflectivity $\varepsilon_{tel}(\lambda)$ of the 54.7-Å telescope was fitted by two half-gaussians joined together at the center of the bandpass; then the full width half maximum $\Delta\lambda$ of the overall modeled bandpass was varied from 0.5 Å to 1.5 Å, and the resulting temperature response kernel was calculated for several values of $\Delta\lambda$. Figure 7 shows how small variations in the width of the bandpass can strongly affect the selectivity of the response kernel.

Even with telescopes that have significant contamination in the temperature response kernel, it is possible to generate images with high-temperature selectivity. After the flight, images from several telescopes can be combined through linear combination, to improve the composite temperature response kernel of the final image. For example, both the 193-Å and the 173-Å Ritchey-Chrétien telescopes on the MSSTA flight show some contamination from nearby oxygen lines. Each telescope has a temperature response kernel that peaks near 10^6 K, with a subsidiary peak near 3×10^5 K. The 150-Å Ritchey-Chrétien has a similarly dual-peaked response kernel. By taking a linear combination of these three kernels, it is possible to produce a composite kernel that is much more sharply peaked at 10^6 K, than any of the original kernels; similarly, a different linear combination produces a relatively sharp peak at 3×10^5 K (see Fig. 8). Pointwise linear combination of images from separate telescopes in the same flight of the MSSTA can be used in this way to produce composite images with greater temperature resolution than an image from any single MSSTA telescope.

Clearly, alignment is crucial to this technique of combining separate solar images. Unless the solar images used in the final combination process are aligned to within less than the effective angular resolutions of the telescopes, the composite temperature response kernel will be poorly defined. For this technique to be successful, good knowledge of the separate telescopes' orientations, resolutions, and plate scales are required.

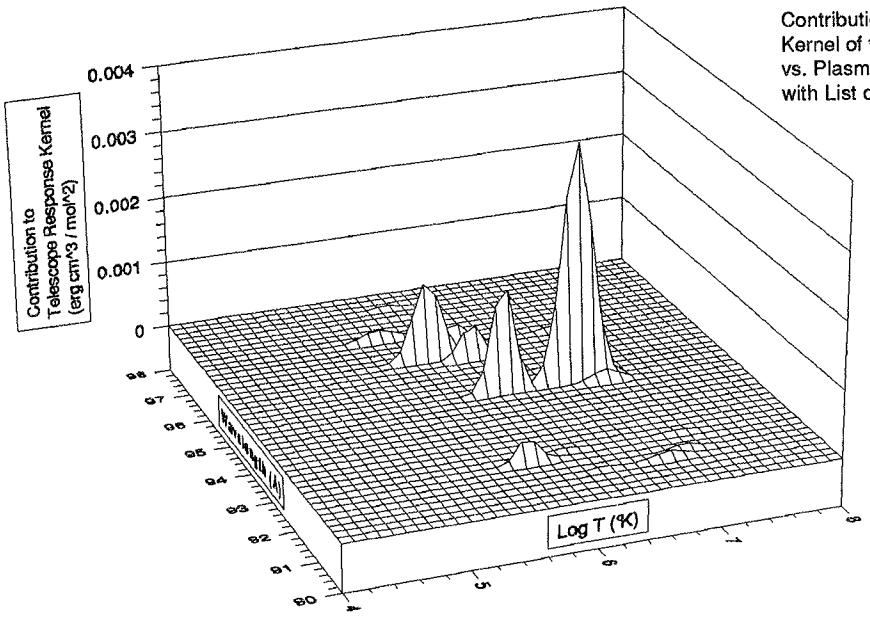

Ion	Wave-length	Rel. Max. Height (%)	Log T at Peak
FE XVIII	93.93	100.0	6.7
FE X	**94.02**	**40.5**	**6.1**
MG VI	*95.48*	*31.3*	*5.7*
FE X	**95.37**	**12.7**	**6.1**
NE VII	*91.56*	*7.9*	*5.7*
FE X	**96.12**	**5.9**	**6.1**
FE XX	93.78	4.8	6.9
SI V	96.44	4.1	5.5
FE IX	94.02	2.8	6.0
FE XIX	91.02	2.7	6.8
FE XXI	91.28	1.9	7.0
NE VII	88.23	1.8	5.8
NE VII	*89.37*	*1.7*	*5.7*
MG V	*95.48*	*1.5*	*5.7*
NI XXI	95.85	1.3	6.9
NI XX	94.49	1.3	6.8
NE VIII	88.08	1.3	5.8

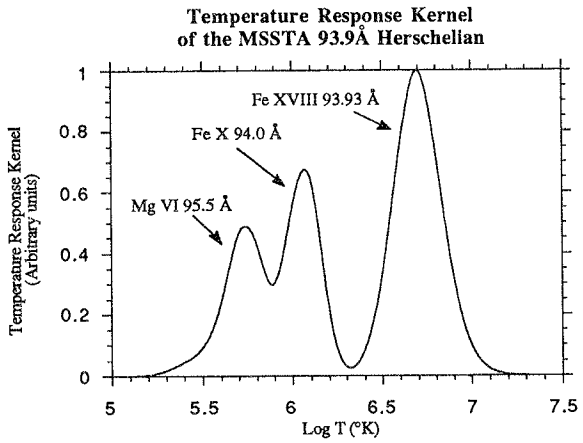

Fig. 4. Contribution to telescope response kernel, vs. temperature and wavelength, for spectral lines near the bandpass peak of the MSSTA 93.9-Å telescope, and the resulting total temperature response kernel. For this telescope, three main lines contribute to the response kernel: Fe XVIII at 93.93 Å, Fe X at 94.0 Å, and Mg VI at 95.5 Å. Because these lines are all strong, and because each has its peak emission at a different temperature, the temperature response kernel is trimodal: the telescope responds nearly as strongly to plasmas near the peak emissivities of Fe X at 1.3×10^6 K and Mg VI at 5.4×10^5 K, as to plasmas at the desired temperature, 5.0×10^6 K, which is the temperature of peak emissivity for the Fe XVIII line at 93.93 Å.

5. CORONAL LOOPS

As an illustration of the MSSTA's utility as a plasma diagnostic tool, the response of the MSSTA to a variety of coronal features has been calculated. Figure 9 shows the theoretical temperature and density profiles of two coronal loops, calculated with the model of Vesecky et al.[11] This example illustrates the ability of the MSSTA to distinguish between features of similar size, shape, and density, but with different temperatures and different coronal heating intensities. Both loops are symmetric arcs, extending 2.5×10^9 cm from footpoint to summit, with radius of curvature 3×10^9 cm and peak density 10^9 cm. Loop no. 1 is heated uniformly at 1.5×10^{-3} erg s^{-1} cm^{-3} and loop no. 2 at 3.7×10^{-3} erg s^{-1} cm^{-3}, resulting in peak temperatures of 2.3×10^6 K and 3.0×10^6 K, respectively.

By fitting theoretically calculated telescope responses to data from digitized images, it will be possible to determine the actual temperature and density profiles of coronal loops, and to discern the magnitude of the coronal heating. Figure 10 shows the responses of the 193-Å and 304-Å Ritchey-Chrétien telescopes to the two theoretical coronal loops. Because these telescopes will resolve a few tenths of an arc second (0.1 arcsec = 7.3×10^6 cm at 1 AU), all of the salient features of the response curves would be easily observed, providing a good temperature diagnostic. Temperature resolution may be further enhanced by the techniques outlined in the previous section.

It has been speculated that coronal loops are heated by many small impulsive events rather than by a steady energy input.[12] If so, then images of loops may show a highly irregular and asymmetric brightness, depending on how the exposure time compares with the time scale of the impulsive heating mechanism. Because thermal conduction is so efficient, it is unlikely that the *spatial* dependence of coronal heating will significantly affect the shapes of the temperature and density curves given in the Fig. 9 example, unless the heating is highly localized, as in

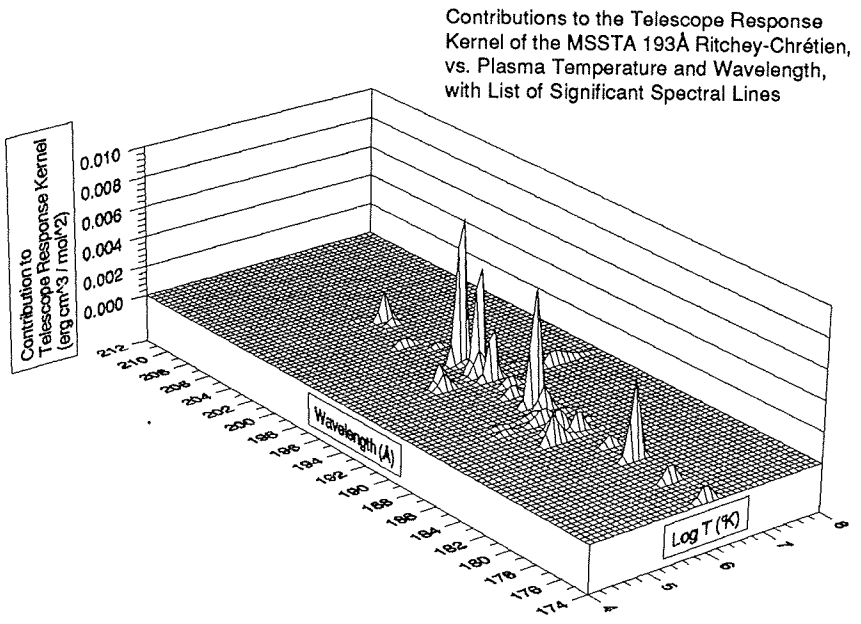

Ion	Wave-length	Rel. Max. Height (%)	Log T at peak
FE XII	**195.13**	**100.0**	**6.2**
FE XI	**188.22**	**79.8**	**6.1**
FE XII	**193.52**	**71.6**	**6.2**
FE XI	**180.41**	**51.3**	**6.1**
FE XII	**192.40**	**33.3**	**6.2**
FE XIII	**202.04**	**20.6**	**6.2**
FE XI	**192.82**	**17.2**	**6.1**
FE XI	**187.45**	**16.6**	**6.1**
O V	*192.90*	*16.4*	*5.4*
O VI	*184.13*	*13.4*	*5.5*
FE X	184.54	13.0	**6.0**
FE VIII	185.23	12.9	5.8
O V	*192.80*	*11.1*	*5.4*
FE X	177.24	10.1	**6.0**
FE XXIV	192.03	9.3	7.2
FE X	174.53	8.9	**6.0**
FE VIII	186.61	8.4	5.8
FE X	190.04	6.7	**6.0**
O VI	183.95	6.6	5.5
FE XI	182.17	6.4	**6.1**
S VIII	198.56	5.3	5.9
S XI	191.26	5.3	**6.2**
FE IX	171.08	5.1	5.9
FE XIII	201.11	4.8	**6.2**

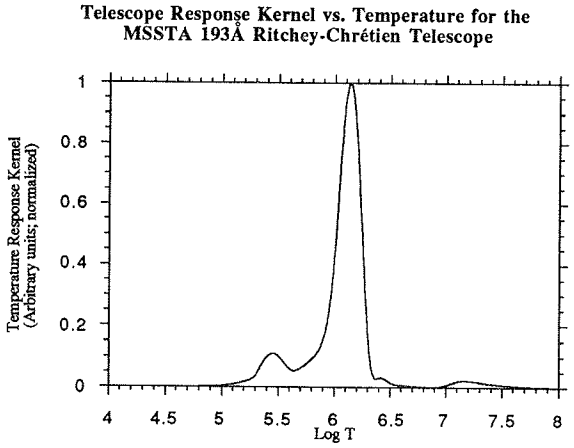

Fig. 5. Contribution to telescope response kernel, vs. temperature and wavelength, for the MSSTA 193-Å Ritchey-Chrétien telescope, and the resulting total temperature response kernel. Note that while there are many contributing lines across the entire bandpass of the telescope, most of them have emissivity curves that peak near the same temperature. Thus, although the telescope "sees" a variety of materials in a variety of ionization states, the temperature response of the telescope is still relatively sharp.

the impulsive heating model. Because the MSSTA telescope exposure time will be relatively short (on the order of a few seconds to a minute), the MSSTA should be able to distinguish between these two models of coronal loop heating.

6. CONCLUSIONS

The analysis of the response of the Ritchey-Chrétien, Cassegrain, and Herschelian telescopes to the solar spectrum indicates that we should meet our objective of obtaining high spatial resolution images that are dominated by emission from the coronal plasma in a narrow temperature range (by isolating XUV bandpasses corresponding to a single emission line or line multiplet) for most of our bandpasses. For those bandpasses that have a significant contribution from the plasma at more than one temperature, we have developed analytical techniques that can extract the single temperature response. The utility of this high-temperature resolution has been theoretically demonstrated with an example of coronal loop analysis.

7. ACKNOWLEDGMENTS

The MSSTA project at Stanford University is supported by NASA grant NSG-5131. Troy W. Barbee, Jr., is supported by the U.S. Department of Energy through Lawrence Livermore National Laboratory under contact W-7405-Eng-48. Richard B. Hoover is supported in part by a grant from the MSFC Center Director's Discretionary Fund and by NASA Grant NSG-5131. We wish to express our gratitude to Terry Dillard and Bob Carter of Morton Thiokol and to Max Sharpe of MSFC for their efforts in producing the filament wound optical benches; to Richard Bell, James R. Williams, and Dale Wasserman of MSFC for design and fabrication support; to Bobby Tidmore, Jerry Rabideau, Neal Deason, and Kendall Coker of Ver-Val for fabricating

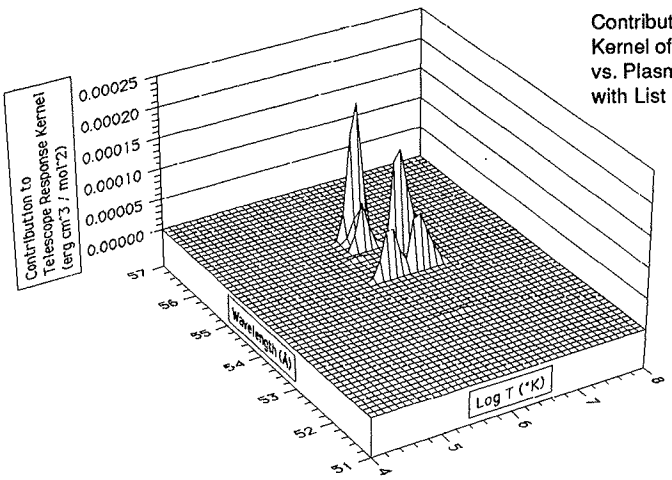

Contributions to the Telescope Response Kernel of the MSSTA 54.7Å Herschelian, vs. Plasma Temperature and Wavelength, with List of Significant Spectral Lines

Ion	Wave-length	Rel. Max. Height (%)	log T at peak
SI IX	55.36	100.0	6.1
FE XVI	**54.70**	**68.4**	**6.4**
FE XVI	**54.15**	**36.2**	**6.4**
MG IX	55.06	31.8	6.0
S VIII	54.12	30.2	5.9
SI IX	55.27	22.9	6.1
FE XV	**54.70**	**14.0**	**6.3**
SI VIII	55.36	7.9	6.0
FE XV	**54.15**	**7.6**	**6.3**
S IX	54.18	7.5	6.1
MG VIII	55.06	5.4	6.0
S VII	54.12	3.7	5.9
SI VIII	55.27	1.8	6.0

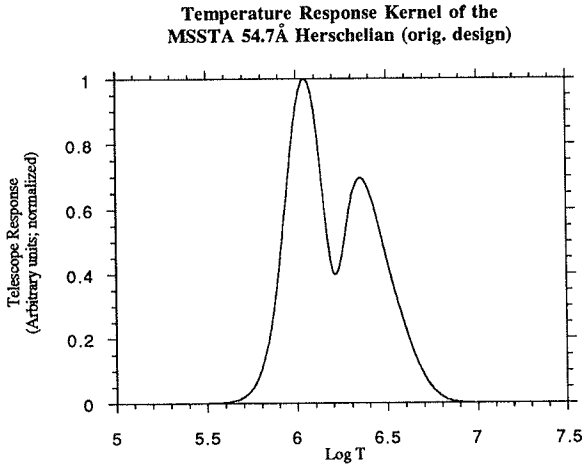

Fig. 6. Original telescope response kernel for the MSSTA 54.7-Å telescope. Note the double-humped shape of the curve, caused by on-band contamination of the desired Fe XVI peak (at roughly 3 million K) by Si IX. Note that the contaminant line actually dominates over the desired Fe XVI line.

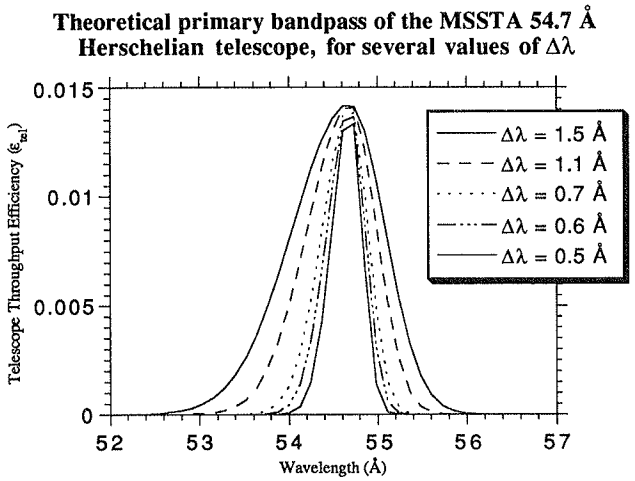

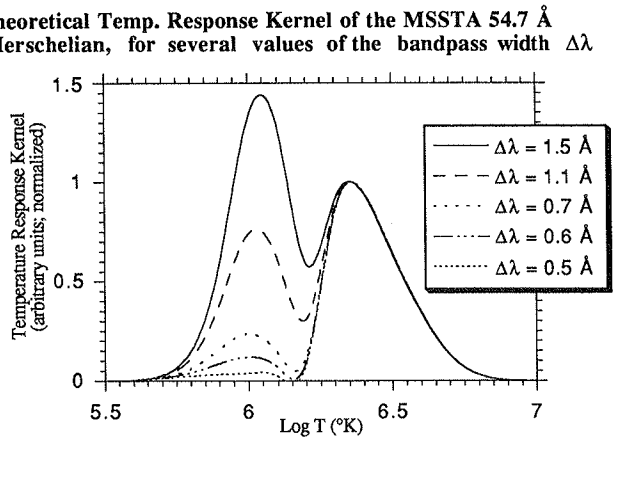

Fig. 7 Theoretical bandpasses and temperature response kernels for several values of the bandpass width Δλ in the 54.7-Å Herschelian. Note the dramatic differences in temperature selectivity that result from relatively small differences in the width of the bandpass.

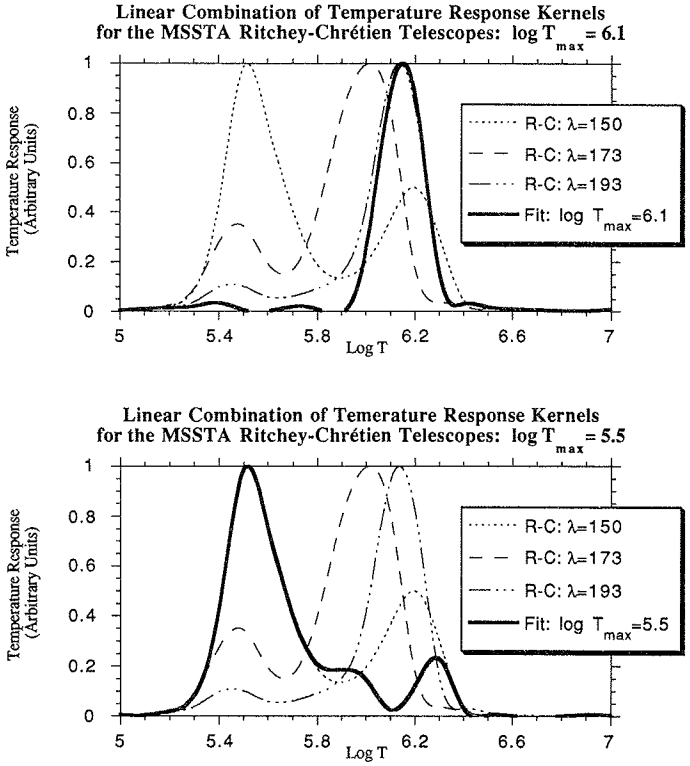

Fig. 8. Linear combination of temperature response kernels for three Ritchey-Chrétien telescopes to produce two different composite response kernels. Each of the composite response kernels is more sharply peaked than any of the three original kernels, each of which is bimodal with a peak near $10^{5.5}$ K and a peak near $10^{6.1}$ K. By selecting linear combinations of the kernels so that one peak was reduced and the other enhanced, more sharply peaked composite kernels were produced. The separate response kernels for the 150-Å, 173-Å, and 193-Å telescopes were multiplied by −0.1, −0.7, and 3.5, respectively, and added and renormalized to produce the curve at the top. The curve at the bottom was produced similarly, but with coefficients of 10.0, 1.6, and −5.0, respectively.

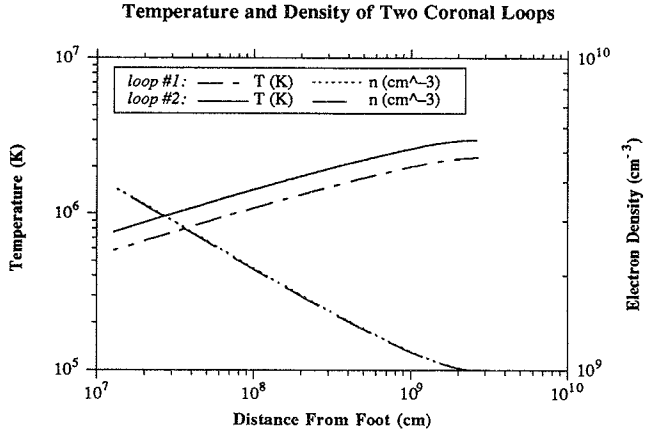

Fig. 9. Numerically calculated temperature and density of two hypothetical coronal loops. The calculation includes thermal conduction, radiative loss, variable cross-sectional loop area, and pressure variation caused by gravity. Coronal heating is assumed to be uniform for this example. The equations were integrated from the top of the loop to the base, so that a peak temperature and density could be specified. The temperature and coronal heating function of the second loop were varied in such a way as to give it the same size as the first.

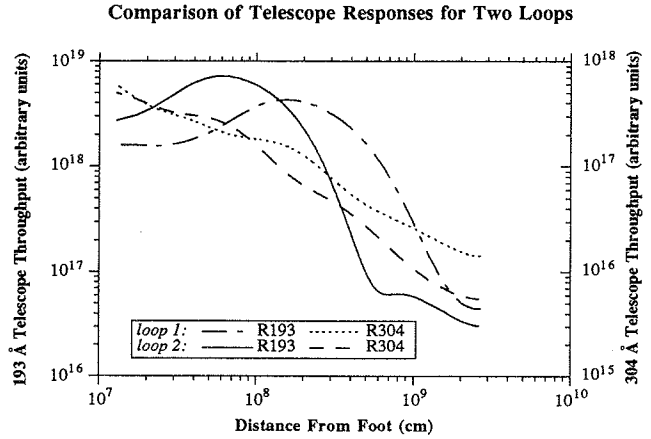

Fig. 10. Response of two of the MSSTA telescopes to the temperature and density profiles of Fig. 9, integrated along the line of sight through the plasma. The response curves are shifted by as much as 100 times the resolution of the telescope for a 25% difference in peak temperatures.

the telescope structures; to Glen Callahan of Acton Research for the fabrication of VUV mirror coatings and filters; to Stephen Powell of Stanford University and Forbes Powell of Luxél for their advice on XUV filters; to Jim Lemen of LPARL for providing the Mewe emissivity data file; to Mitch Furst, Randy Canfield, and Bob Madden of NIST for support during our calibration measurements; to James Hadaway and Cynthia Peterson of the University of Alabama, Huntsville, and Johnny Lyle and Terry Lee of Ver-Val for assistance with the interferometric measurements; and to Piero Pianetta for assistance with the measurements at SSRL.

8. REFERENCES

1. A. B. C. Walker, Jr., J. F. Lindblom, R. H. O'Neal, M. J. Allen, T. W. Barbee, Jr., and R. B. Hoover, "The Multispectral Solar Telescope Array," *Opt. Eng.*, 29(6), 582 (1990).
2. J. B. Hadaway, H. B. Johnson, R. B. Hoover, J. F. Lindblom, and A. B. C. Walker, Jr., "Design and analysis of optical systems for the Stanford/MSFC Multi-Spectral Solar Telescope Array," *Proc. SPIE* 1160, 195–208 (1989); R. B. Hoover, P. C. Baker, J. B. Hadaway, R. B. Johnson, C. Peterson, D. R. Gabardi, A. B. C. Walker, Jr., J. F. Lindblom, C. E. DeForest, and R. H. O'Neal, "Performance of the Multi-Spectral Solar Telescope Array III: optical characteristics of the Ritchey-Chrétien and Cassegrain Telescopes," *Proc. SPIE* 1343, 189 (1990).
3. A. B. C. Walker, Jr., J. F. Lindblom, R. B. Hoover, and T. W. Barbee, Jr., "Monochromatic x-ray and XUV imaging with multilayer optics," *Journal de Physique Colloque* C1 49, pp C1-175–C1-186 (1988).
4. R. G. Athay, "Radiation output," in *Physics of the Sun*, P. A. Sturrock, T. E. Holzer, D. M. Mihalos, and R. K. Ulrich, eds., 2, 29, D. Reidel Publishing Co., Dordrecht (1985).
5. A. B. C. Walker, Jr., "Interpretation of the x-ray spectra of active regions," in *Solar Gamma X- and EUV Radiation*, Proc. IAU Symposium No. 68, Buenos Aires, S. R. Kane, ed., pp. 73–100, D. Reidel Publishing Co., Dordrecht (1975).
6. R. Mewe, E. H. B. M. Gronenschild, and G. H. J. van den Oord, "Calculated X-radiation from optically thin plasmas. V.", *Astron. Astrophys. Suppl. Ser.* 62, 197–254 (1985).
7. M. Landini and B. C. Monsignori Fossi, "The X-UV spectrum of thin plasmas," *Astron. Astrophys. Suppl. Ser.* 82, 229–260 (1990).
8. T. W. Barbee, Jr., J. W. Weed, Jr., R. B. Hoover, R. H. O'Neal, J. F. Lindblom, A. B. C. Walker, Jr., J. R. Roberts, E. B. Saloman, and T. W. Barbee III, "Performance of the Multi-Spectral Solar Telescope Array II: The multilayer mirrors," in *X-Ray/EUV Optics for Astronomy, Microscopy, Polarimetry, and Projection Lithography*, R. B. Hoover and A. B. C. Walker, Jr., eds., *Proc. SPIE* 1343 (1991).
9. Joakim F. Lindblom, Ray H. O'Neal, Arthur B. C. Walker, Jr., Forbes R.

Powell, Troy W. Barbee, Jr., Richard B. Hoover, and Stephen F. Powell, "The Multi-Spectral Solar Telescope Array IV: the soft x-ray and extreme ultraviolet filters," *Opt. Eng.* 30(8), 1134–1141 (1991).
10. R. B. Hoover, T. W. Barbee, Jr., P. C. Baker, J. F. Lindblom, M. J. Allen, C. DeForest, C. Kankelborg, R. O'Neal, E. S. Paris, and A. B. C. Walker, Jr., "Performance of compact multilayer coated telescopes at soft x-ray/EUV and far ultraviolet wavelengths," *Opt. Eng.* 30(8) (1991).
11. J. F. Vesecky, S. K. Antiochos, and J. H. Underwood, "Numerical modeling of quasi-static coronal loops," *Astrophys. J.* 233, 987–997 (1979).
12. P. A. Sturrock, W. W. Dixon, J. A. Klimchuk, and S. K. Antiochos, "Episodic coronal heating," *Astrophys. J. Lett.* 356, L31–L34 (June 1990).

Maxwell J. Allen: Biography and photograph appear with the paper "Multi-Spectral Solar Telescope Array II: soft x-ray/EUV reflectivity of the multilayer mirrors" in this issue.

Joakim F. Lindblom: Biography and photograph appear with the paper "Multi-Spectral Solar Telescope Array IV: the soft x-ray and extreme ultraviolet filters" in this issue.

Ray H. O'Neal: Biography and photograph appear with the paper "Multi-Spectral Solar Telescope Array II: soft x-ray/EUV reflectivity of the multilayer mirrors" in this issue.

Arthur B.C. Walker, Jr.: Biography appears with the paper "Multi-Spectral Solar Telescope Array II: soft x-ray/EUV reflectivity of the multilayer mirrors" in this issue.

Troy W. Barbee, Jr.: Biography and photograph appear with the paper "Multi-Spectral Solar Telescope Array II: soft x-ray/EUV reflectivity of the multilayer mirrors" in this issue.

Richard B. Hoover: Biography and photograph appear with the guest editorial in this issue.

Biographies and photographs for other authors not available.

Multi-Spectral Solar Telescope Array IV: the soft x-ray and extreme ultraviolet filters

Joakim F. Lindblom, MEMBER SPIE
Ray H. O'Neal
Arthur B. C. Walker, Jr., MEMBER SPIE
Stanford University
Center for Space Science and Astrophysics
Stanford, California 94305

Forbes R. Powell, MEMBER SPIE
Luxel Corporation
Friday Harbor, Washington 98250

Troy W. Barbee, Jr., MEMBER SPIE
Lawrence Livermore National Laboratory
Livermore, California 94550

Richard B. Hoover, MEMBER SPIE
NASA Marshall Space Flight Center
Space Science Laboratory
Huntsville, Alabama 35812

Stephen F. Powell, MEMBER SPIE
Stanford University
Department of Material Science and Engineering
Stanford, California 94305

Abstract. The multilayer mirrors used in the normal-incidence optical systems of the Multi-Spectral Solar Telescope Array (MSSTA) are efficient reflectors for soft x-ray/extreme ultraviolet (EUV) radiation at wavelengths that satisfy the Bragg condition, thus allowing a narrow band of the soft x-ray/EUV spectrum to be isolated. However, these same mirrors are also excellent reflectors in the visible, ultraviolet, and far-ultraviolet (FUV) part of the spectrum, where normal incidence reflectivities can exceed 50%. Furthermore, the sun emits far more radiation in the ultraviolet and visible part of the spectrum than it does in the soft x-ray/EUV. For this reason, thin foil filters are employed to eliminate the unwanted longer wavelength solar emission. With the proper choice of filter materials, the filters can also be used to eliminate EUV radiation at longer wavelengths, where the increasing specular reflectivity of multilayer mirrors and the high intensity of solar emissions can cause "contamination" of the image in the narrow band defined by the Bragg condition. In addition, filters can eliminate higher order multilayer reflections. Finally, filter absorption edges can sometimes be utilized to reduce the width of the primary bandpass. The MSSTA instrument uses various combinations of thin foil filters composed of aluminum, carbon, tellurium, potassium bromide, beryllium, molybdenum, rhodium, and phthalocyanine to achieve the desired radiation rejection characteristics. We discuss issues concerning the design, manufacture, and predicted performance of MSSTA filters.

Subject terms: x-ray/EUV optics; x-ray filters; x-ray windows; thin metal foils.

Optical Engineering 30(8), 1134-1141 (August 1991).

CONTENTS

1. INTRODUCTION

The wavelength-selective property of multilayer mirrors constitutes a powerful tool for astronomical observations of extreme ultraviolet (EUV) and soft x-ray sources. However, most astronomical soft x-ray/EUV sources are also luminous at other wavelengths [particularly in the far ultraviolet (FUV), ultraviolet (UV), and visible], where multilayer optics are unable to eliminate unwanted radiation. If the detector being used is sensitive at these wavelengths, then this radiation must be attenuated before it reaches the focal plane. In most cases, attenuation can be done by adding broadband filters to the optical path. In addition, with careful choice of filter materials, the same broadband filter can be used to reduce or to eliminate certain types of unwanted soft x-ray/EUV radiation (such as higher order multilayer reflections or contamination from longer wavelength EUV radiation that is specularly reflected by the multilayer optics). Due to the high absorption coefficients of most materials in the soft x-ray/EUV, these filters must be made extremely thin, typically less than 1 μm thick. Thin foils such as these, in the size range required ($\geqslant$100 mm^2), necessitate special precautions in their manufacture, mounting, and use.[1,2]

The function of thin foil filters for use with soft x-ray/EUV multilayer optics can be loosely divided into four categories:

1. Eliminate visible, UV, and FUV radiation.
2. Reduce the contribution from specular reflection at wavelengths longward of the telescope bandpass.
3. Eliminate higher-order reflections from multilayer mirrors.
4. Make the primary bandpass narrower with the help of absorption edges.

To illustrate these functions, we look first at a representative astronomical soft x-ray/EUV source spectrum (the sun) and the characteristics of a typical multilayer mirror. Figures 1(a) through 1(c) show typical solar spectra as measured by Malinovsky and

Invited paper XR-106 received Jan. 10, 1991; revised manuscript received March 20, 1991; accepted for publication March 22, 1991. This paper is a revision of paper 1343-51 presented at the SPIE conference X-Ray/EUV Optics for Astronomy, Microscopy, Polarimetry, and Projection Lithography, July 1990, San Diego, Calif. The paper presented there appears (unrefereed) in SPIE Proceedings Vol. 1343.